1 **B**est Practices in **P**hysics-based Fault Rupture Models for **S**eismic **H**azard **A**ssessment of **N**uclear **I**nstallations: issues and challenges towards full Seismic Risk Analysis

Cadarache-Château, France, 14-16 May 2018

ID_28

NONLINEAR BEHAVIORS AND STRUCTURAL DAMPING IDENTIFICATION IN REINFORCED CONCRETE ELEMENTS

T. HEITZ[1,2], C. GIRY[1], A. LE MAOULT[3], B. RICHARD[3], F. RAGUENEAU[1]

[1]LMT, ENS Cachan, CNRS, Université Paris–Saclay, 61, avenue du Président Wilson, F-94235, Cachan, France.

[2]OSE-Engineering, Chemin de Cabestany à Villelongue, F-66000, Perpignan, France.

[3]CEA–DEN, Service d'études mécaniques et thermiques (SEMT), Université Paris–Saclay, F-91191, Gif-sur-Yvette, France.

Email of contact of main author: ragueneau@lmt.ens-cachan.fr

Abstract. Despite their now well documented drawbacks, viscous damping based models to describe the dissipations occurring in reinforced concrete (RC) structures during seismic events are popular among structural engineers. Their computational efficiency and their convenient implementation and identification are indeed attractive. Of course, the choice of a viscous damping model is, most of the time, reasonable, but some questions still arise when it comes to calibrate its parameters. To address this problem, a numerical study based on an experimentally identified structural model is here presented. To this end, an experimental campaign has been carried out on RC beams set up on the AZALEE shaking table of the TAMARIS experimental facility operated by the French Alternative Energies and Atomic Energy Commission (CEA). This work takes place in the scope of a moderate seismicity context for which steel yielding is not expected. An evolving equivalent viscous damping ratio estimated for a simply supported reinforced concrete beam is proposed. The results are not directly identified from experimental results but rather from numerical simulations carried out thanks to an equivalent single-degree-of-freedom model, itself calibrated by means of quasi-static experiments. In this paper, the experimental campaign is first presented. Then, the single-degree-of-freedom model and the identification procedure are exposed. The resulting outputs are presented and commented. Finally, numerical experiments are performed in order to obtain equivalent viscous damping ratio values corresponding to a given maximum time-history curvature and a curvature demand.

Key Words: Dissipations; Reinforced concrete; Viscous damping; Experimental campaign

1. Introduction

The ability of a structure to withstand a seismic event is driven by its capability to store and/or dissipate the input energy without compromising its integrity. Even though available material constitutive laws are now able to provide realistic and accurate results about the nonlinear behavior of RC, the computational cost is a strong counterpart that designers and engineers are rarely prone to pay for when dealing with full-scale structures. In practice, an additional viscous damping is often used to account for dissipations not taken into account by the structural model [1, 2]. Before performing such a fine analysis, simplified methodologies should be used in order to obtain a first design of a structure. In this case, the equivalent viscous damping ratio (EVDR) has a key role when assessing maximum structural responses (i.e. reduction of the demand spectra to integer the nonlinearities of the structure) and some studies show it is the second source of uncertainties after the ground motions [3, 4]. Nevertheless, this assumed equivalence with the energy dissipated hysteretically may be questionable. Indeed, several studies have emphasized

2   **Best** Practices in **P**hysics-based Fault Rupture Models for **S**eismic **H**azard **A**ssessment of **N**uclear **I**nstallations: issues and challenges towards full Seismic Risk Analysis

Cadarache-Château, France, 14-16 May 2018

ID_28

the fact that the viscous damping depends on the response amplitude for RC buildings [5–7] and on their degradation state often described by a displacement ductility level[8–14]. In fact, there is actually no reason to keep the EVDR constant throughout the nonlinear time-history analysis (NLTHA). To sum-up, the aforementioned papers suggest that the EVDR depends on the degradation state of the structure and on the displacement demand. The influence of both parameters is investigated in this paper which focuses on weak to moderate earthquakes which do not induce steel yielding in structures. In particular, it is considered that the main dissipations occur in the concrete (e.g. crack initiation, propagation and friction). To investigate these aspects, an experimental campaign has been set up on RC beams by means of the AZALÉE shaking table, as part of the TAMARIS experimental facility operated by the French Alternative Energies and Atomic Energy Commission (CEA). The main objective is to provide the scientific and engineering communities reference data through both dynamic and quasistatic tests in order to evaluate the dissipations depending on structural, material and signal characteristics. In the first section, the experimental campaign is described and explained thoroughly. Then, the calibration of the beam equivalent single-degree-of-freedom (SDOF) model and the EVDR assessment method are presented. Then, the SDOF model formulation and its identification procedure are detailed. Finally, numerical experiments are performed on this model in order to obtain EVDR values corresponding to a maximum relative history displacement and a relative displacement demand.

2. Experimental campaign

2.1. Framework

In the framework of SINAPS@ project [15], the IDEFIX experimental campaign took place in the TAMARIS experimental facility at the French Alternative Energies and Atomic Energy Comission (CEA) from May to November 2016. Twenty RC beams have been casted and their dimensions have been designed in order to make their first two eigenmodes being in the optimally-controlled frequency range of the shaking table, *Azalée*, i.e. under 30 Hz according to IDEFIX boarded mass. The experimental protocol ensures the acquisition of relevant data to estimate degradations and energy dissipations in and at the boundaries of the structure.
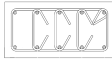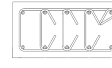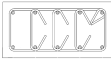
The choice has been made to design a campaign that includes the main types of loadings (quasi-static, low and high level dynamic) performed on elements that are more simply modeled than others, i.e. beams. Ambient seismic noise based methods require long duration recording to counterbalance the poor signal-to-noise ratio. For this reason, the authors have decided not to use them.

2.2. Specimens

The specimens are six-meter long RC beams with a cross-section of 20 cm × 40 cm. Two concrete classes, two steel reinforcements types and three different diameters are chosen to design a total of six designs of specimens listed in table 1. A typical beam weights around 1150 kg. For the sake of clarity, each beam has been labeled with respect to its characteristics (i.e. type of reinforcement and concrete):

- The two steel reinforcements types are ribbed B500B steel bars following european stan-

3 **Best** Practices in **P**hysics-based Fault Rupture Models for **S**eismic **H**azard **A**ssessment of **N**uclear **I**nstallations: issues and challenges towards full Seismic Risk Analysis

Cadarache-Château, France, 14-16 May 2018

ID_28

TABLE 1: Different beam designs

Label	HA20-C1A	HA16-C1A	HA12-C1A
Pattern design			
Pattern label	4HA20	8HA16	4HA12
$\rho^{(1)}(\%)$	1.57	2.01	1.41
$S_b^{(1)}(\text{cm}^2\cdot\text{m}^{-1})$	25.1	40.2	37.7
Steel label	HA20	HA16	HA12
$f_s^{(1)}(\text{MPa})$	>560[2]	568	528
$E_s^{(1)}(\text{GPa})$	237	217	206
Concrete label	C1A	C1A	C1A
Concrete class	C25/30	C25/30	C25/30
$f_{c,28d}^{(1)}(\text{MPa})$	35.0	35.0	35.0
$f_{c,6m}^{(1)}(\text{MPa})$	36.9	36.9	36.9
$E_{c,28d}^{(1)}(\text{GPa})$	26.4	26.4	26.4
$E_{c,6m}^{(1)}(\text{GPa})$	26.2	26.2	26.2
Label	HA12-C1B	RL12-C1B	HA12-C2
Pattern design			
Pattern label	4HA12	4RL12	4HA12
$\rho^{(1)}(\%)$	1.41	1.41	1.41
$S_b^{(1)}(\text{cm}^2\cdot\text{m}^{-1})$	37.7	37.7	37.7
Steel label	HA12	RL12	HA12
$f_s^{(1)}(\text{MPa})$	528	468	528
$E_s^{(1)}(\text{GPa})$	206	218	206
Concrete label	C1B	C1B	C2
Concrete class	C25/30	C25/30	C45/55
$f_{c,28d}^{(1)}(\text{MPa})$	29.7	29.7	45.4
$f_{c,6m}^{(1)}(\text{MPa})$	33.0	33.0	47.4
$E_{c,28d}^{(1)}(\text{GPa})$	28.7	28.7	29.2
$E_{c,6m}^{(1)}(\text{GPa})$	28.1	28.1	28.2

[1] ρ: reinforcement ratio – S_b: interface surface – f_y: steel yield stress – E_s: steel Young's modulus – $f_{c,28d}$: concrete strength at 28 days – $f_{c,6m}$: concrete strength at 6 months – $E_{c,28d}$: Concrete Young's modulus at 28 days – $E_{c,6m}$: Concrete Young's modulus at 6 months.
[2] Maximum force capacity of the testing machine reached

dards (norm BS 4449, conforming to the Eurocode 2 [16]) labeled HA (standing for "high adherence") and round steel bars labeled RL. The three different diameters are 12 mm, 16 mm and 20 mm. The reinforcement patterns are described in table 1 and will be later labeled in a shorter way (respectively): HA12, RL12, HA16 and HA20. The reinforcement ratios of 10HA12, 10RL12 and 4HA20 are close while the one of 8HA16 is higher. Similarly, 10HA12, 10RL12 and 8HA16 have a close interface surface (i.e. surface of the steel-concrete bond, idealized as a cylinder with a diameter equal to the nominal diameter of the reinforcement) while the one of 4HA20 is lower.

- Two concrete classes have been formulated, they correspond to C25/30 and C45/55 classes as defined in Eurocode 2 section 3.1.2 [16] and are labeled respectively C1 and C2 for this campaign. Two casts were necessary for the concrete C1 and they proved to have different mechanical properties. This motivates the choice to distinguish two variants of C1, namely C1A and C1B.

4   **Best** Practices in **P**hysics-based Fault Rupture Models for **S**eismic **H**azard **A**ssessment of **N**uclear **I**nstallations: issues and challenges towards full Seismic Risk Analysis

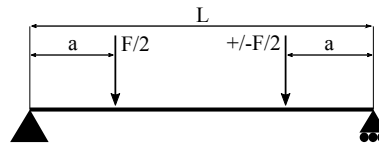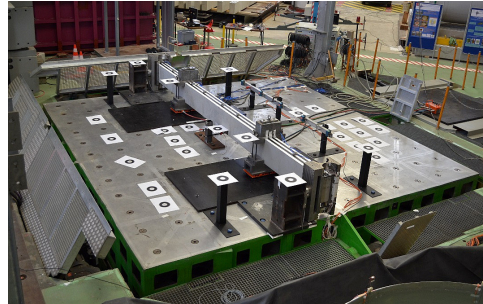Cadarache-Château, France, 14-16 May 2018

ID_28

FIG. 1: Configuration of the quasi-static tests, with $L = 5.9$ m and $a = \frac{L}{4}$

(a) Setup on strong floor

(b) Setup on *Azalée*

FIG. 2: IDEFIX experimental setup on the strong floor (a) and on the shaking table (b)

2.3.   Strong floor tests

Eight beams have been tested on a strong floor in a four-point bend configuration (figure 1) with two hydraulic cylinders of 25 kN capacity each, a maximum velocity of 1.6 m·s⁻¹ and a maximum displacement of ±120 mm. The choice of a 4PB test is made in order to better approximate the first two modes shapes thanks to the actuators (more details are given regarding this point in section 2.7.1).
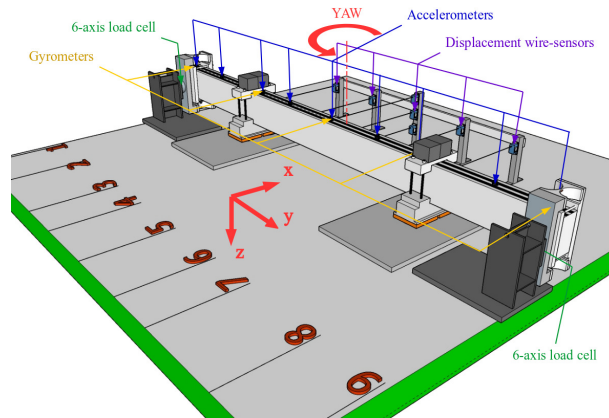
2.4.   Shaking table tests

The twelve other beams have been tested on *Azalée* shaking table which measures 6 m × 6 m. The particularity of this equipment is its ability to move in three translations and three rotations.
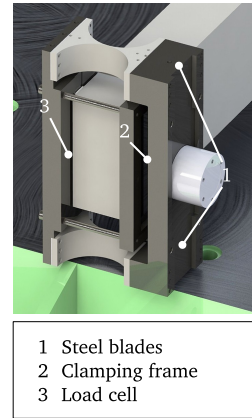
2.5.   Boundary conditions and additional masses

The beam-end supports consist in elastic "blades" (figure 3b) mounted in parallel in order to free the rotation of the beam around the vertical axis without inducing spurious friction mechanisms. High-performance steel (Marval 18H®, yield stress $R_{p,0.2\%}$ = 1860 MPa and Young's modulus E = 186 GPa) has been used and allows the thinnest part of these blades for being only 2.5 mm thick. Another originality regarding the boundary conditions is the use of air cushions at both quarter-spans in order to bear the whole weight of the setup while drastically reducing the friction with the floor. Additional masses of 350 kg are also mounted on the air cushions to fulfill the requirements regarding the first two eigenfrequencies (see section 2.1).

5 **Best** Practices in **P**hysics-based Fault Rupture Models for **S**eismic **H**azard **A**ssessment of **N**uclear **I**nstallations: issues and challenges towards full Seismic Risk Analysis

Cadarache-Château, France, 14-16 May 2018

ID_28

(a) 3D view of the sensors setup and working basis
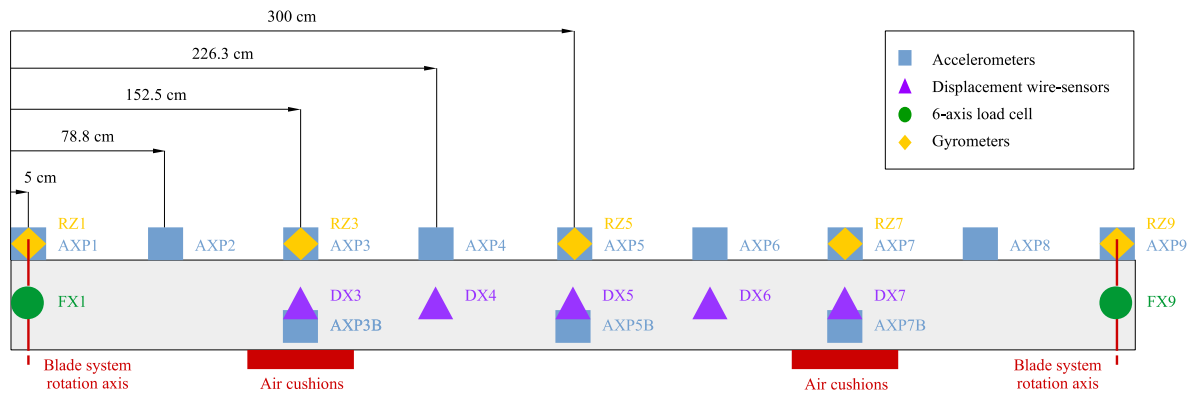
(b) Blades beam supports

FIG. 4: Schematic view of the sensors setup

2.6. Measurements

A variety of sensors is used to build a strong database for each test:

- 5 displacement wire sensors;

- an industrial digital image correlation tool (Videometric®[17]) to track the mid-plane of the beam along the tests;

- 5 gyrometers (to measure the rotational velocity);

- 19 accelerometers;

- 2 six-axis load cells at the beam supports;

- 2 monoaxial load cells on cyclinders.

The sensors setup is described in both figures 3a and 4. Nine reference positions which divide the beam in eight equal parts. Then, each sensor is labeled with respect to its position number (from 1 to 9). The black stripes painted on the upper surface of the beam are tracked by the DIC tool which provides a discretized full field measurement of the beam's mid-plane transverse displacement $u(t_j, x_k)$ at time $t_{j \in [\![1, N_t]\!]}$ and at position $x_{k \in [\![1, N_x]\!]}$, $x_{N_x} = L$ being the

6 **Best** Practices in **P**hysics-based Fault Rupture Models for **S**eismic **H**azard **A**ssessment of **N**uclear **I**nstallations: issues and challenges towards full Seismic Risk Analysis

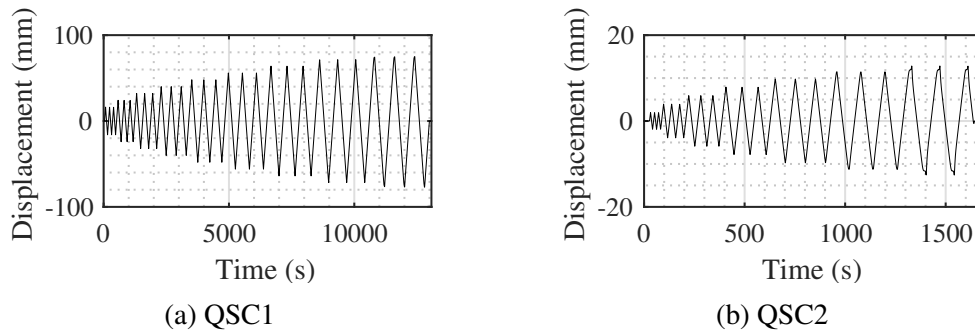Cadarache-Château, France, 14-16 May 2018

ID_28

FIG. 5: Actuator prescribed displacement for QSC1 and QSC2 (at quarter-span)

span of the beam. The linear combination v of the N_m[th] first flexural mode shapes, which best approximates the measured one u, is sought:

$$v(t,x) = \sum_i^{N_m} a_i(t) \cdot f_i(x) \tag{1}$$

where the f_i are the flexural mode shapes and the a_i are the modal coordinates. More details are given in a dedicated paper [18].

2.7. Overview of the loadings

Table 2 shows an overview of the different loadings which have been tested on the beams during the experimental campaign.

2.7.1. Quasi-static loadings

There are four different quasi-static loadings. The two firsts, QSC1 and QSC2, are reverse cyclic tests. The displacement amplitude grows by blocks of three cycles as plotted in figure 5, and the loading velocity is 0.4 mm·s^{-1}. The fundamental difference between these two loadings is that the actuators are either in-phase or in phase-opposition. The purpose of these tests is to evaluate the EVDR associated to the first two flexural eigenmodes, that is, QSC2 prescribes a displacement that will create a deformed shape close to the second mode shape of the beam. The 4-point bending creates an area of constant bending moment in the part of the beam between both actuators. It generates in this area a relatively homogeneous stress/strain state, allowing for reasoning in terms of fracture energy per RC volume. However, it could be argued that 3-point bending would initiate internal friction due to transverse shear forces. For practical (experimental setup), time reason and economical reasons, this participation to the dissipations has not been investigated, but it would represent an interesting addition to IDEFIX experimental campaign.

2.7.2. Dynamic loadings

Dynamic signals sent on the shaking table command unit are either broad band (white noises, or bandpassed white noises) or harmonic. Advantages are taken from the ability of

7   **Best** Practices in **P**hysics-based Fault Rupture Models for **S**eismic **H**azard **A**ssessment of **N**uclear **I**nstallations: issues and challenges towards full Seismic Risk Analysis

Cadarache-Château, France, 14-16 May 2018

ID_28

TABLE 2: Descriptions of the loadings

Equipment	Reference	Eigenmodes	Description
	HT	1 and 2	Hammer test
	WN1	1	White noise signal in X-direction (duration 200 s)
	WN2	2	White noise signal around YAW-axis (duration 200 s)
	WN3	1 and 2	White noise signal (combination of WN1 and WN2)
	WN1MTS	1	White noise genereted by MTS software
	WND030	1	White noise of table displacement bandpassed between 0 Hz and 30 Hz
	SC1	1	White noise signal in X-direction bandpassed between $0.5 \cdot f_1$ and $1.05 \cdot f_1$, f_1 being the first eigenfrequency
	SC2	2	White noise signal in YAW-direction bandpassed between $0.5 \cdot f_2$ and $1.05 \cdot f_2$, f_2 being the second eigenfrequency
	SC2b	2	White noise signal in YAW-direction bandpassed between $0.35 \cdot f_2$ and $1.05 \cdot f_2$, f_2 being the second eigenfrequency
Azalée	SC12	1 and 2	Combination of SC1 and SC2
	SS1	1	Natural seismic signal, transfered at third floor spectrum of Niigataken-Chuetsu-Oki earthquake (NCOE)
	Sinus	1 or 2	Sinusoidal signal in X-direction or around YAW-axis
	DSSf_1f_2	1 or 2	Harmonic signal at constant amplitude, by decreasing frequency steps (from f_1 to f_2) in X-direction or around YAW-axis
	ISD	1	Step-by-step increasing sinusoidal acceleration following a quadratic law (i.e. a linearly increasing displacement demand)
	BS	1	Continuous linear sinus sweep generated by MTS software
	QSS025	1	Continuous quadratic sinus sweep generated by MTS software
	BiSINUS	1 and 2	Sinusoidal signals consecutively in X, X+YAW and YAW directions
	QSC1	1	Quasi-static reverse cyclic four-point bend test with in-phase actuators
	QSC2	2	Quasi-static reverse cyclic four-point bend test with actuators in phase opposition
Strong floor	SPS1	1	Quasi-static reverse cyclic four-point bend test with in-phase actuators and increasing velocity (constant velocity during one cycle)
	SPS2	2	Quasi-static reverse cyclic four-point bend test with actuators in phase opposition and increasing velocity (constant velocity during one cycle)

the table to move simultaneously in two different directions (e.g. along X and/or around YAW for IDEFIX tests). Indeed, the second eigenmode of the beam (i.e. S-shaped mode) is difficult to activate because of the symmetrical construction of the experimental setup. The acceleration on YAW-DOF creates inertial forces in opposite directions on beam and additional masses from each side of table's vertical rotation axis. In order to reach similar levels of excitation for both DOF, an equivalence of absolute acceleration along X-axis at the hinges is chosen. Hence, equation (2) links the rotational acceleration θ_g on YAW-DOF and the acceleration a_g along

8 **Best** Practices in **P**hysics-based Fault Rupture Models for **S**eismic **H**azard **A**ssessment of **N**uclear **I**nstallations: issues and challenges towards full Seismic Risk Analysis

ID_28
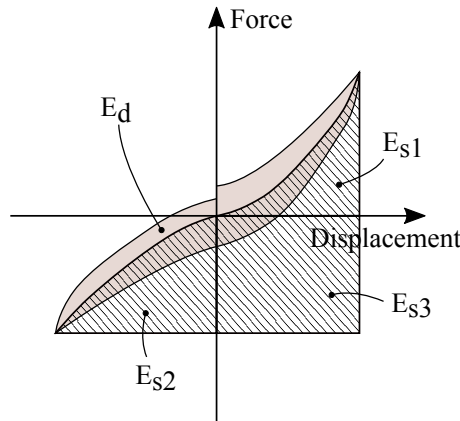
Cadarache-Château, France, 14-16 May 2018

FIG. 6: Nonlinearly stored energy evaluated on a full-cycle inspired by [20]

X-DOF (with L the distance between the two hinges).

$$\theta_g = \frac{2 \cdot a_g}{L} \tag{2}$$

3. Equivalent viscous damping identification procedure

A viscous damping model is a convenient — yet not totally satisfying — way to represent the dissipations occurring in a RC structure on which a dynamic loading is applied. Jacobsen [19] proposed a method to assess an optimal equivalent viscous damping ratio from an energetic point of view by showing that:

$$\xi = \frac{1}{2 \cdot \pi} \cdot \frac{\omega_0}{\omega} \cdot \frac{E_d}{E_s} \tag{3}$$

with E_d the energy dissipated by the viscous damper during one displacement half-cycle Γ_u starting at $t = 0$ and ending at $t = \frac{\pi}{\omega}$ and E_s the maximum stored elastic energy reached at displacement U. This method should be used cautiously taking into the remarks recalled in the authors' papers [18]. A graphical interpretation of this method modified with inspiration from the work of Kumar et al. [20] in given in figure 6.

4. Identification of an hysteretic model on experimental data

4.1. Quasi-static cyclic reverse test

A quasi-static cyclic reverse loading, labeled QSC1, is carried out thanks to two actuators mounted at positions $\frac{L}{4}$ and $\frac{3 \cdot L}{4}$ with an increasing cycle amplitude. Each cycle of this displacement-driven loading is repeated three times to stabilize the damage state of the beam. The corresponding time-displacement evolution is given in figure 7. In order to construe the whole displacement response of the beam as the one of a simple degree of freedom oscillator (SDOF), a full-field measurement based upon a commercial digital image correlation method has been used (Videometric [17]). This method provides displacement data all along the beam, allowing for the projection over the eigenmode shapes [18, 21]. In the present case, the presented displacement data result from the projection of the displacement field of the beam on the theoretical first mode shape computed thanks to a finite element model of the experimen-

9 **Best** Practices in **P**hysics-based Fault Rupture Models for **S**eismic **H**azard **A**ssessment of **N**uclear **I**nstallations: issues and challenges towards full Seismic Risk Analysis

ID_28
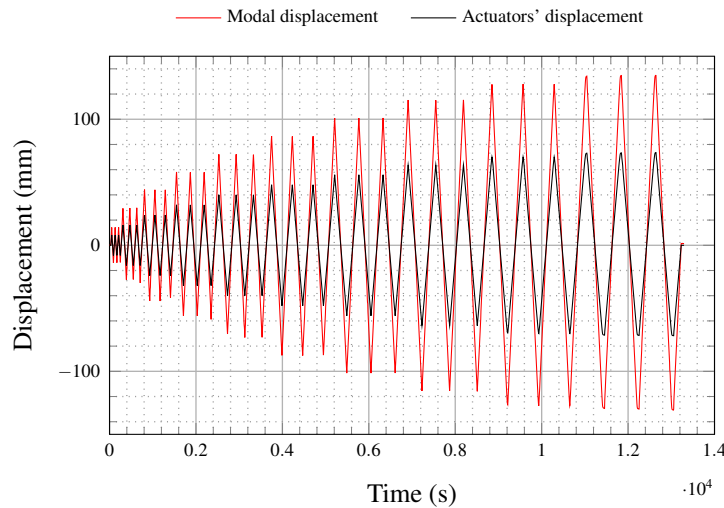
Cadarache-Château, France, 14-16 May 2018

FIG. 7: Imposed actuators' displacement and resulting modal displacement of the experimental QSC1 loading
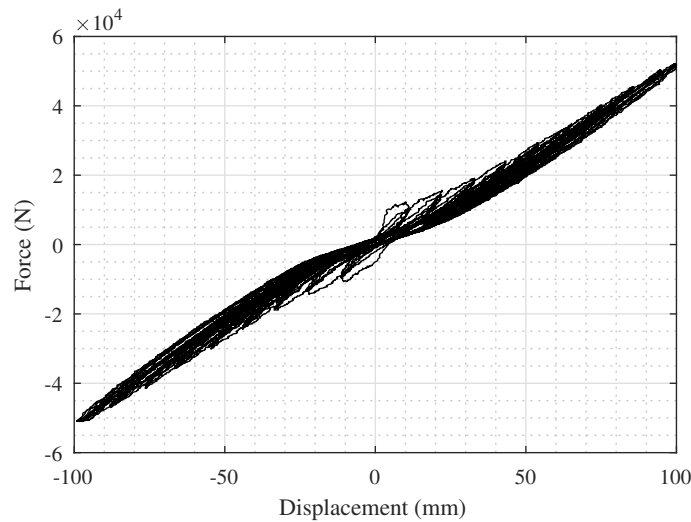

FIG. 8: Force-displacement measurement for the considered QSC1 test

tal setup. Thus, they can be considered as an estimation of the first mode displacement. The corresponding force-displacement graph is represented in figure 8.

4.2. Formulation of a SDOF hysteretic model for the beam behavior

4.2.1. Objectives

In order to describe the behavior of the beam, a nonlinear oscillator is associated to the first eigenmode. This model is not intended to be general but rather adapted to the QSC1 test (i.e. bending of the beam following the first mode shape). It provides a useful basis for numerical experiments that will be carried out on virtual quasi-static tests in section 5. These numerical experiments investigate the uncoupled influence of both the loading amplitude (e.g. displacement, curvature, force, bending moment) and degradation state.
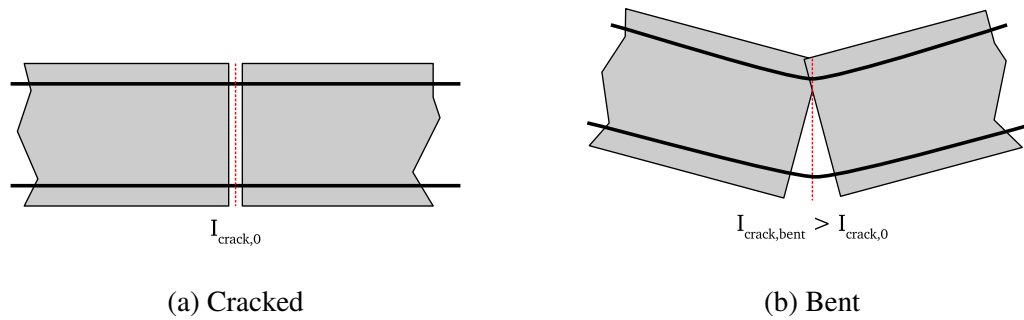
10 **Best** Practices in **P**hysics-based Fault Rupture Models for **S**eismic **H**azard **A**ssessment of **N**uclear **I**nstallations: issues and challenges towards full Seismic Risk Analysis

Cadarache-Château, France, 14-16 May 2018

ID_28

| (a) Cracked | (b) Bent |

FIG. 9: Illustration of the increase of moment of inertia due to crack closure under bending

4.2.2. Modeled phenomena

The model presented in this section strongly relies on the work of Moutoussamy [22]. For small displacements applied at the initial state, the beam in bending has a linear elastic behavior, i.e. has a constant stiffness K which can be identified. Beyond a limit displacement δ_y, the beam starts to exhibit nonlinearities. A stiffness decrease is observed during the unloading phase, this indicates the creation and propagation of cracking and motivates the use of the damage mechanics framework [23].

Steel yielding is not observed during the tests and is consequently not taken into account. Nevertheless, hysteresis loops are observed during loading-unloading cycles. It is explained by the existence of friction within the reinforced concrete, e.g. between cracks surfaces or between the steel reinforcements and the surrounding cracked concrete. Hence, a sliding displacement variable u^π is defined [24, 25].

The unilateral effect is taken into account by splitting each internal variable related to damage in two parts. These parts correspond to two allegedly independent families of cracks on upper or lower half cross-sections of the beam from either side of the neutral axis depending on the direction of deflection. Supposing a linear behavior of concrete in compression, the beam behavior is mainly driven by the tension area (and the associated damage state). The index i will be used to stand for both direction indexes "+" and "−". A kinematic hardening variable α^π is associated to the friction displacement u^π.

Finally, the last observed phenomenon is the so-called "pinching" effect which consists in a stiffness reduction in the neighborhood of the zero-displacement point that explains the reversed S-shape of the load displacement curve. The origin of this effect is not clearly understood but different hypotheses exist. Several researchers state that this effect indicates a failure driven by shear [26–32]. However, a shear failure is unlikely to occur with such a flexible beam in four-point bending test. Hence, two explanations are here proposed:

- in the case of a crossing crack, the crack surfaces get into contact when the displacement is high enough (as illustrated on figure 9) thus enlarging the virtual cross section of the beam at the crack location;

- the steel-concrete bond failure induces slipping until the adherence is found again at the interface (inter-locking).

A complete theoretical description of the model is given in an article to be submitted or can alternatively be found in its first version (with minor differences) in a conference paper [33].

11 **Best** Practices in **P**hysics-based Fault Rupture Models for **S**eismic **H**azard **A**ssessment of **N**uclear **I**nstallations: issues and challenges towards full Seismic Risk Analysis

Cadarache-Château, France, 14-16 May 2018

ID_28

Mechanism	Observable variable	Internal variable
Displacement	u	
Damage		d_i
Friction		u^π
Kinematic hardening		α^π
Crack closure		η

TABLE 3: Internal variables of the model

Notation	Description	Value	Unit
δ_y	Yield displacement	6.4	mm
K_0	Initial stiffness	1.88	N·mm⁻¹
p	Stiffness loss coefficient	0.228	–
q	Fragility coefficient	0.426	–
a^π	Hysteresis loops width	1480	N
b^π	Initial stiffness of the hysteresis loops	74.7	N·mm⁻¹
U_c	Crack closure displacement	54.2	mm

TABLE 4: Model parameters and identified values

4.2.3. Model identification

The model identification is performed thanks to a minimization algorithm applied on the global relative force error ε_F given in equation (4). More details on the identification procedure are given in a paper to be submitted. The effects of the different parameters are graphically described on figures 10.

$$\varepsilon_F = \sum_{i=1}^{N} \frac{\left(F_i^e - F_i^{exp}\right)^2}{\left(F_i^{exp}\right)^2} \tag{4}$$

The identification results are summarized in table 4 and the corresponding error indicator of equation 4 equals $\varepsilon_F = 0.0376$.

(a) Parameters influence for a monotonic loading

(b) Parameters influence for a unilateral cyclic loading (without pinching)

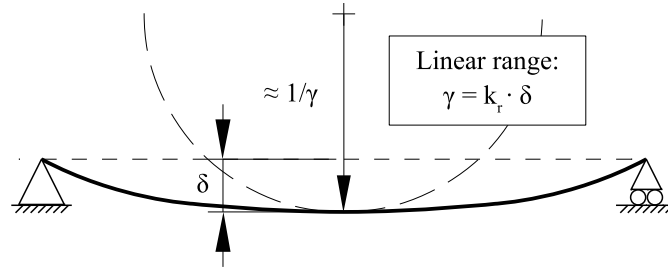FIG. 10: Description of some parameters influence on the model behavior

12 **Best** Practices in **P**hysics-based Fault Rupture Models for **S**eismic **H**azard **A**ssessment of **N**uclear **I**nstallations: issues and challenges towards full Seismic Risk Analysis

ID_28

Cadarache-Château, France, 14-16 May 2018

FIG. 11: Displacement and curvature as engineering demand parameters

5. Numerical study of the EVDR dependence on engineering demand parameters

5.1. Engineering demand parameters

The dependence of the EDVR on the degradation and loading levels are investigated. The choice is made in this paper to select the mid-span curvature γ (see figure 11) as the quantity of interest to quantify the loading level. Also, a degradation index Γ is defined as the maximum historic curvature measured at mid-span γ_m over the theoretical first steel yielding curvature γ_y as expressed in equation (7).

The curvature has the advantage over the displacement to be bending-type independent (e.g. 3-point or 4-point bending) since it is defined at the most critical section. Moreover, γ_y can be computed in a predictive way on the basis of design rules (such as Eurocode 2 [16]) knowing the material and geometrical properties of the RC section. A multifiber finite element simulation allows for the estimation of the curvature–mid-span displacement law in equation (5). Considering a Eurocode 2-type constitutive law for the concrete, a linear evolution of the curvature as function of the mid-span deflection is obtained:

$$\gamma = k_r \cdot \delta \qquad (5)$$
$$\text{with} \quad k_r = 0.2707 \text{ m}^{-3} \qquad (6)$$

The details of this result are given in [18]. The value of steel-yielding curvature numerically obtained for the studied beam is given in equation (8). It is recalled that the dissipations associated to steel yielding are not in the scope of this study. Hence, Γ is expected to remain within the range $[0, 1]$.

$$\Gamma = \frac{\gamma_m}{\gamma_y} \qquad (7)$$
$$\text{with} \quad \gamma_y = 0.0298 \text{ m}^{-1} \qquad (8)$$

The study of the influence of the degradation level and of the loading on the EVDR is challenging for pragmatic reasons. A cyclic quasi-static reverse test as QSC1 takes about 4 hours to perform (not counting the setup phase). Then, the testing for many degradation states could be very time-consuming. When practical constraints (for example related to the schedule, the cost, or the available equipment) make impossible to investigate experimentally the influence of different parameters on a quantity of interest numerical experimentation represents an elegant way to address the problem, under the condition that the numerical model used has been validated experimentally. Considering the ability of the model identified in section 4.2.3 to represent the phenomena taking place during the bending, it can be used as support of virtual quasi-static testing.
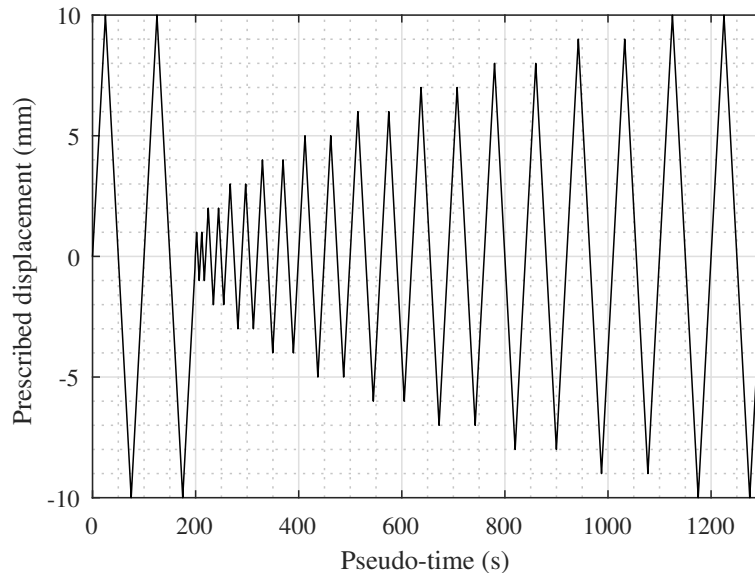
13 **Best** Practices in **P**hysics-based Fault Rupture Models for **S**eismic **H**azard **A**ssessment of **N**uclear **I**nstallations: issues and challenges towards full Seismic Risk Analysis

ID_28

Cadarache-Château, France, 14-16 May 2018

FIG. 12: Loading procedure for the sensitivity study (example for $\Gamma = 0.091$)

Run	δ_m (cm)	Γ	δ_1 (cm)	δ_2 (cm)	δ_3 (cm)	...	δ_N (cm)
1	0.2	0.018	0.2				
2	0.3	0.027	0.2	0.3			
3	0.4	0.036	0.2	0.3	0.4		
...	...	...	...	...	...	...	
N	10.0	0.91	0.2	0.3	0.4	...	10.0

TABLE 5: Loading procedure with increasing degradation index – δ_m: maximum displacement; δ_i: amplitude of i$^{\text{th}}$ block

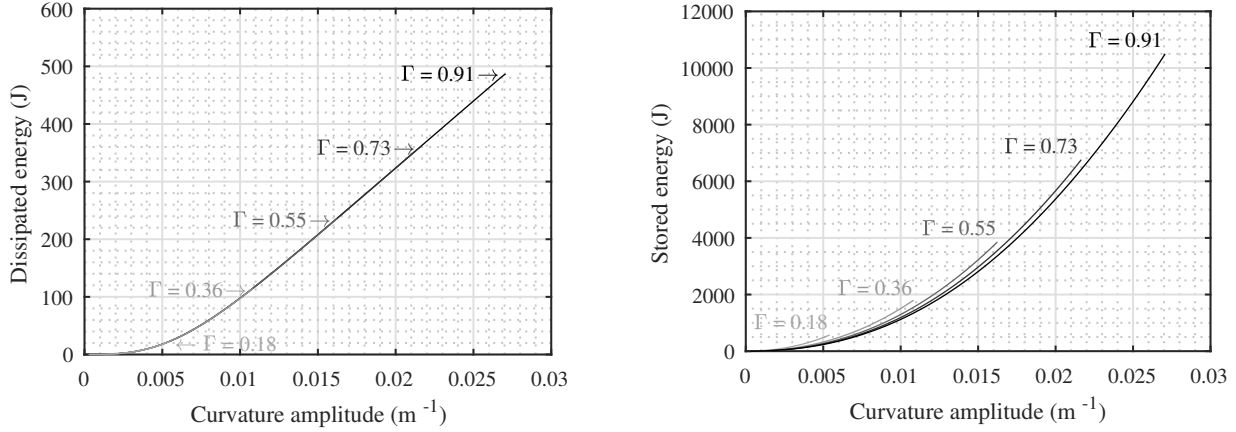## 5.2. Influence of the degradation and loading levels

5.2.1. Numerical loading

As a side positive consequence for the use of a virtual experimental, there is no spurious dissipation due to external sources. Hence, the validity of the representation of hysteretic dissipation by an equivalent viscous damper is assessed. To study the influence of the degradation level Γ and of the prescribed curvature amplitude of the cycle γ, an increasing cyclic reverse quasi-static displacement loading has been designed and is illustrated on figure 12. Each cycle of displacement amplitude δ is repeated twice so the hysteretic behavior in the 2$^{\text{nd}}$ cycle can be considered as stabilized and the energy dissipation due to damage initiation is not taken into account. It is important to note that the first two cycles are equal to the last two in order to remain at the same degradation index Γ of the beam all along the loading.

### 5.2.2. Observations resulting from the numerical simulations

It is clear from the results given in section 5 that the degradation index Γ and the displacement amplitude play a major role in the EVDR. Moreover, these two parameters are model-

14 **B**est **P**ractices in **P**hysics-based **F**ault **R**upture **M**odels for **S**eismic **H**azard **A**ssessment of **N**uclear **I**nstallations: issues and challenges towards full Seismic Risk Analysis

ID_28

Cadarache-Château, France, 14-16 May 2018

(a) Influence of the cycle amplitude on the dissipated energy E_d per cycle for different degradation indexes Γ

(b) Influence of the cycle amplitude on the stored energy per cycle E_s for different degradation indexes Γ
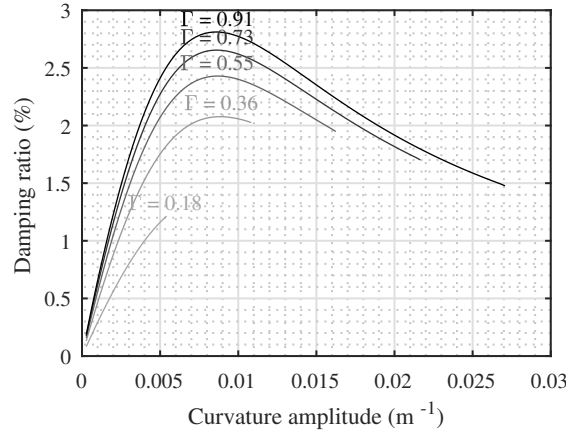
(c) Influence of the cycle amplitude on the equivalent viscous damping ξ_{eq} ratio for different degradation indexes Γ

FIG. 13: Influence of the degradation index γ over energies and equivalent viscous damping ratio ξ_{eq} for different cycle amplitudes obtained by Jacobsen's areas method
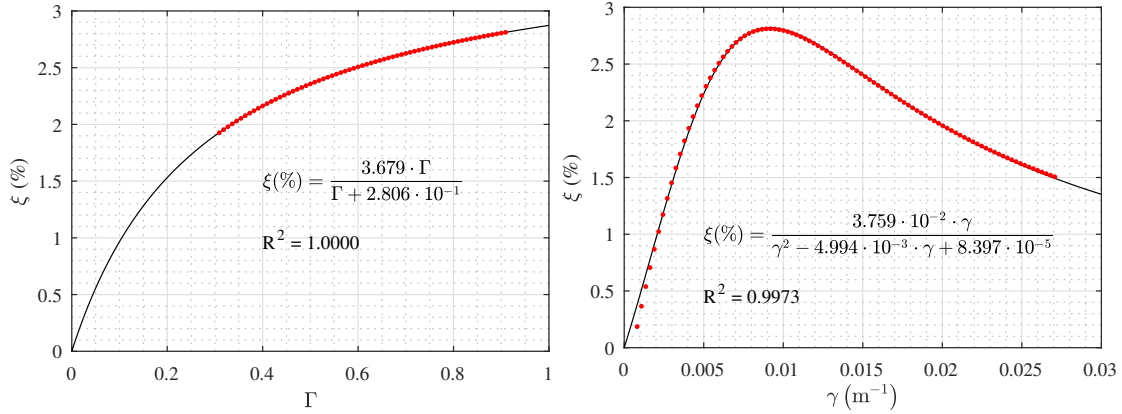
independent. It is possible to plot a cloud of points of EVDR depending on both Γ and displacement amplitude γ as with the red dots on figure 15a. The model includes damage mechanisms, hence, the maximum elastic energy storage decreases with the degradation index Γ (figure 13b). The other important observation is that the energy dissipated does not seem to depend on Γ for the present nonlinear model. However, since the equivalent viscous damping ratio depends on the ratio of the dissipated energy over the stored one, the EVDR seems to increase with respect to the degradation index (see figure 13c).

One can guess a relatively smooth surface fitting the EVDR points. Then, the highest EVDR point is chosen as the "identification" point of coordinates $(\Gamma_{id}, \gamma_{id}, \xi_{id})$ and identified on figure 15a for the next steps:

- $\Gamma = \Gamma_{id}$ is fixed at this point, and the best-fitting function $g(\gamma)$ is identified (thanks to a nonlinear least squares algorithm implemented in the curve fitting toolbox of Matlab) as on figure 14a:

$$f(\Gamma) = \frac{3.679 \cdot \Gamma}{\Gamma + 0.2806} = \begin{cases} 0\,\% & \text{if } \Gamma = 0 \\ 3.679\,\% & \text{if } \Gamma \to +\infty \end{cases} \tag{9}$$

15 **Best** Practices in **P**hysics-based Fault Rupture Models for **S**eismic **H**azard **A**ssessment of **N**uclear **I**nstallations: issues and challenges towards full Seismic Risk Analysis

ID_28

Cadarache-Château, France, 14-16 May 2018

(a) Identified dependence between EVDR and degradation index for a curvature amplitude $\gamma = 0.009204 \text{ m}^{-1}$

(b) Identified dependence between EVDR and curvature amplitude for a degradation index $\Gamma = 0.73$

FIG. 14: Uncoupled identification of dependence between EVDR, degradation index and curvature amplitude

- $\gamma = \gamma_{id}$ is fixed at this point, and the best-fitting function $f(\Gamma)$ is identified as on figure 14b:
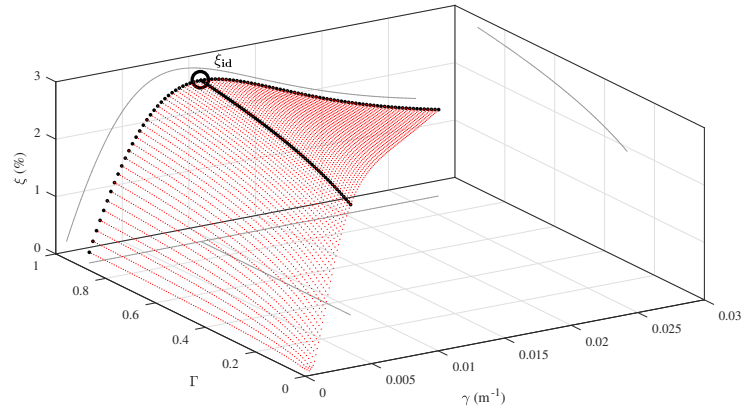
$$g(\gamma) = \frac{0.03759 \cdot \gamma}{\gamma^2 - 0.004994 \cdot \gamma + 8.397 \cdot 10^{-5}} = \begin{cases} 0\ \% & \text{if } \gamma = 0 \\ 0\ \% & \text{if } \gamma \to +\infty \end{cases} \qquad (10)$$

- the surface given by equation $\xi = \alpha \cdot f(\Gamma) \cdot g(\gamma)$ where $\alpha = \frac{1}{\xi_{id}}$ is a normalization coefficient:
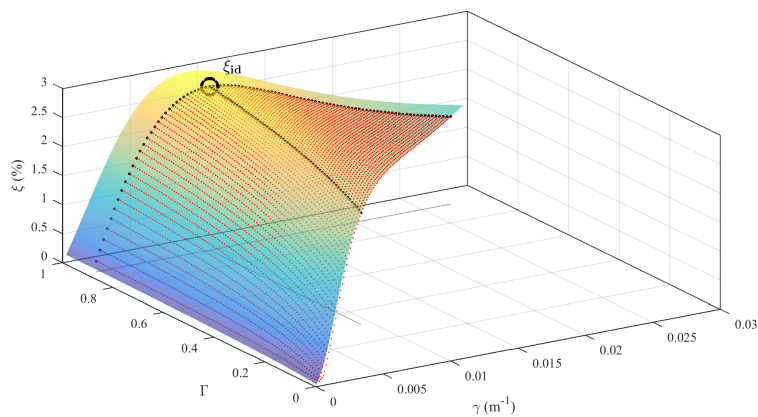
$$\xi(\Gamma, \gamma) = \underbrace{\frac{1}{2.81}}_{\alpha} \cdot \underbrace{\frac{3.679 \cdot \Gamma}{\Gamma + 0.2807}}_{f(\Gamma)} \cdot \underbrace{\frac{0.03962 \cdot \gamma}{\gamma^2 - 0.003403 \cdot \gamma + 7.644 \cdot 10^{-5}}}_{g(\gamma)} \qquad (11)$$

The search for an equation of surface in the form of a product of rational functions is motivated by the form of the expression of the EVDR evaluated by Jacobsen's areas method as a ratio between two energies. The degrees of these polynomial functions are deduced from the shape the curved guessed from the red dots on figures 14a and 14b.

The resulting surface is plotted on figure 15b, and the so-called "damping surface" fits very well the numerical experiments as seen on figure 16. Even though this paper focuses on one particular beam (HA12-C1B), several beam designs have been tested as explained in section 2.2. The model proposed in section 4.2 is able to reproduce the behavior of these different designs because the phenomena involved are the same. The parameters identified are different though, and this results in slightly different shapes of the damping surfaces. However, their overall aspects remain the same.

16 **Best** Practices in **P**hysics-based Fault Rupture Models for **S**eismic **H**azard **A**ssessment of **N**uclear **I**nstallations: issues and challenges towards full Seismic Risk Analysis

Cadarache-Château, France, 14-16 May 2018

ID_28

(a) EVDR values from numerical simulations

(b) Same as figure 15a with superposed fitted surface

FIG. 15: EVDR values for an increasing degradation index Γ and curvature amplitude γ — ξ_{id} represents the identification point for uncoupled functions plotted on figures 14a and 14b; the black dots correspond to the data used for the functions identification of equations 9 and 10
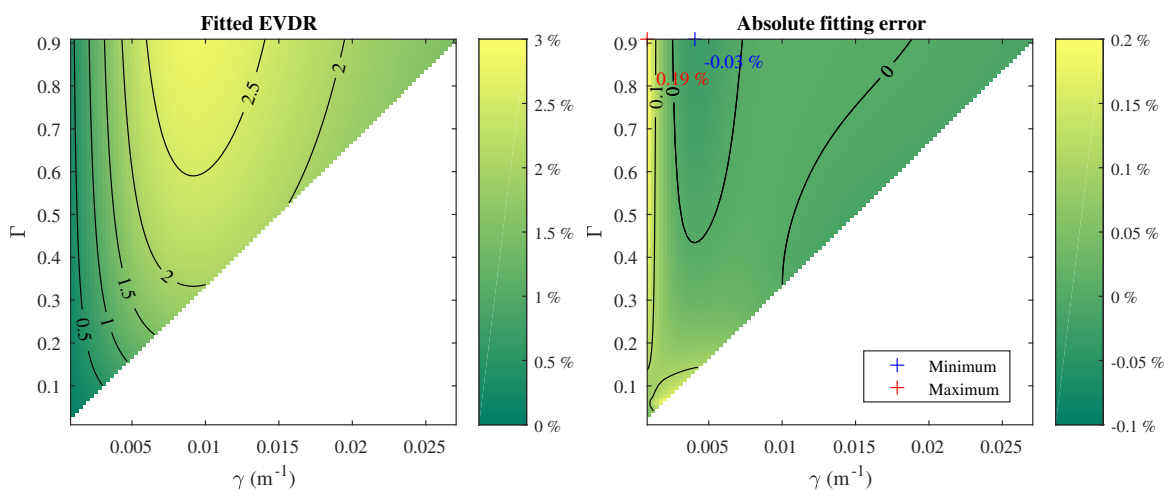
(a) EVDR(%) values from numerical simulations (b) Absolute error of EVDR(%) between the fitted surface and the numerical simulations

FIG. 16: Comparison of the EVDR estimated from the numerical simulations and the corresponding values on the best-fitting surface (interpolated on the identification domain)

17 **Best** Practices in **P**hysics-based Fault Rupture Models for **S**eismic **H**azard **A**ssessment of **N**uclear **I**nstallations: issues and challenges towards full Seismic Risk Analysis

Cadarache-Château, France, 14-16 May 2018

ID_28

6. Conclusions

In order to improve the relevancy of simplified nonlinear time-history analysis by enhancing the additional viscous damping term, an experimental campaign has been carried out on reinforced concrete beams in both quasi-static and dynamic tests. In particular, a RC beam has been subject to a quasi-static reverse cyclic four-point bending test. Then, a single-degree-of-freedom model has been proposed and identified to reproduce the experimental restoring force for a prescribed modal displacement measured thanks to a dedicated image correlation based technique. This model has been used to perform additional numerical tests in order to assess both the influence of a degradation index Γ and the amplitude of the curvature at mid-span γ due to the displacement prescribed by the actuators. It is observed that both parameters have a major influence on the equivalent viscous damping. More specifically, the equivalent viscous damping ratio (EVDR) increases with degradation index Γ in an asymptotically way to a theoretical maximum EVDR. However, the evolution of the EVDR as a function of the curvature amplitude is not monotonous: a maximum is reached before the EVDR decreases asymptotically to zero. A function resulting from the product of the two previously identified ones sums-up these observations. It corresponds to the equation of a smooth surface which can be used as a virtual abacus for a more predictive choice of EVDR. At this point of this study, it seems important to take into account the variations of EVDR during the nonlinear time-history analysis since this value can evolve from almost 0 % to 3 % for the studied RC beam. It is worthy noting that the steel yielding is not taken into account in this model, while it is a highly dissipating phenomenon. Many studies focusing on the dissipations related to steel yielding during earthquakes are found in the literature, often proposing an EVDR evolving with respect to the displacement ductility. Hence, the work carried out in this paper is intended to be complementary to these models. The next step of this study will be to use the damping surface as a basis for a fast and physical-wise updating strategy for the EVDR during nonlinear time-history analyses.

Acknowledgments

References

[1] Frédéric Ragueneau, Jacky Mazars, and Christian La Borderie. Damage model for concrete including residual hysteretic loops: application to seismic and dynamic loading. *FraMCos-3*, pages 685–696, 1998.

[2] Romain Crambuer, Benjamin Richard, Nicolas Ile, and Frédéric Ragueneau. Experimental characterization and modeling of energy dissipation in reinforced concrete beams subjected to cyclic loading. *Engineering Structures*, 56:919–934, 2013.

[3] Ozan Cem Celik and Bruce R Ellingwood. Seismic fragilities for non-ductile reinforced

18 **Best** Practices in **P**hysics-based Fault Rupture Models for **S**eismic **H**azard **A**ssessment of **N**uclear **I**nstallations: issues and challenges towards full Seismic Risk Analysis

Cadarache-Château, France, 14-16 May 2018

ID_28

concrete frames Role of aleatoric and epistemic uncertainties. *Structural Safety*, 32(1):1–12, 2010.

[4] Sang Hyun Lee, Kyung Won Min, Jae Seung Hwang, and Jinkoo Kim. Evaluation of equivalent damping ratio of a structure with added dampers. *Engineering Structures*, 26(3):335–346, 2004.

[5] Q. S. Li, K. Yang, N. Zhang, C. K. Wong, and A. P Jeary. Field measurements of amplitude-dependent damping in a 79-storey tall building and its efects on the structural dynamic responses. *The Structural Design of Tall Buildings*, 11(2):129–153, 2002.

[6] Kun Sung Liu and Yi Ben Tsai. Observed natural frequencies, damping ratios, and mode shapes of vibration of a 30-story building excited by a major earthquake and Typhoon. *Earthquake Spectra*, 26(2):371–397, 2010.

[7] Naoki Satake, Ken-ichi Suda, Toshiharu Arakawa, Atsushi Sasaki, and Yukio Tamura. Damping evaluation using full-scale data of buildings in Japan. *Journal of Structural Engineering*, 129(4):470–477, 2003.

[8] E. Rosenblueth and I Herrera. On a kind of hysteretic damping. *Journal of Engineering Mechanics*, (90):37–48, 1964.

[9] Polat Gulkan and Mete A Sozen. Inelastic responses of reinforced concrete structure to earthquake motions. *Journal Proceedings*, 71(12):604–610, 1974.

[10] Wilfred D. Iwan and Nathan C Gates. The effective period and damping of a class of hysteretic structures. *Earthquake Engineering and Structural Dynamics*, 7(3):199–211, 1979.

[11] M. J Kowalsky. Displacement based design: a methodology for seismic design applied to RC bridge columns. Technical report, University of California, 1994.

[12] M. J Nigel Priestley. *Myths and fallacies in earthquake engineering, revisited*. IUSS press, 2003.

[13] Abdelsamie Elmenshawi and Tom Brown. Hysteretic energy and damping capacity of flexural elements constructed with different concrete strengths. *Engineering Structures*, 32(1):297–305, jan 2009.

[14] Hugo Rodrigues, Humberto Varum, António Arêde, and Aníbal Costa. A comparative analysis of energy dissipation and equivalent viscous dampung of RC columns subjected to uniaxial and biaxial loading. *Engineering Structures*, 35:149–164, 2011.

[15] SEISM Paris-Saclay Institute. SINAPS@.

[16] Comité Européen de Normalisation. Eurocode 2: Design of concrete structures – Part 1-1: General rules and rules for buildings. Technical Report February 2015, CEN, 2005.

[17] Videometric. Videometric: http://www.videometric.com/en/. Technical report, 2018.

[18] Thomas Heitz, Alain Le Maoult, Benjamin Richard, Cédric Giry, and Frédéric Ragueneau. Dissipations in reinforced concrete components: static and dynamic experimental identification strategy. *Engineering Structures*, (Under review), 2018.

19 **Best** Practices in **P**hysics-based Fault Rupture Models for **S**eismic **H**azard **A**ssessment of **N**uclear **I**nstallations: issues and challenges towards full Seismic Risk Analysis

Cadarache-Château, France, 14-16 May 2018

ID_28

[19] Lydik S Jacobsen. Damping in composite structures. *Proceedings of the 2nd world conference on on earthquake engineering*, 2:1029–1044, 1960.

[20] Shiv Shankar Kumar, Murali Krishna, and Arindam Dey. Cyclic Response of Sand Using Stress Controlled Cyclic Triaxial Tests. *50th INDIAN GEOTECHNICAL CONFERENCE*, (December), 2015.

[21] Thomas Heitz, Benjamin Richard, Cédric Giry, Frédéric Ragueneau, and Alain Le Maoult. Damping identification and quantification: experimental evidences and first numerical results. In *16th World Conference on Earthquake Engineering*, Santiago de Chile, 2017.

[22] Laurent Moutoussamy. *Essais hybrides en temps réel sur structures de Génie Civil*. PhD thesis, Ecole Normale Supérieure de Cachan, 2014.

[23] Jean Lemaître. *A course on damage mechanics*. Springer Berlin Heidelberg, Berlin, Heidelberg, second edition, 1996.

[24] Frédéric Ragueneau. *Fonctionnement dynamique des structures en béton - Influence des comportements hystérétiques locaux*. PhD thesis, École Normale Supérieure de Cachan, 1999.

[25] Benjamin Richard and Frédéric Ragueneau. Continuum damage mechanics based model for quasi brittle materials subjected to cyclic loadings: Formulation, numerical implementation and applications. *Engineering Fracture Mechanics*, 98(1):383–406, 2013.

[26] Russell H. Brown and James O Jirsa. Reinforced Concrete Beams Under Load Reversals. *ACI Journal Proceedings*, 68(5):380–390, may 1971.

[27] J. Penzien and M Celebi. Experimental Investigation into the Seismic Behavior of Critical Regions of Reinforced Concrete Components as Influenced by Moment and Shear. *Earthquake Engineering Research Center, Report*, (73-4), 1973.

[28] V.V. Bertero and E.P Popov. Seismic Behavior of Ductile Moment-Resisting Reinforced Concrete Frames. *Special Publication*, 53:247–292, jan 1977.

[29] Shunsuke Otani. Nonlinear dynamic analysis of reinforced concrete building structures. *Canadian Journal of Civil Engineering*, 7:333–344, 1980.

[30] Angelo D'Ambrisi and Filip C Filippou. Modeling of Cyclic Shear Behavior in RC Members. *Journal of Structural Engineering*, 125(10):1143–1150, oct 1999.

[31] Elizabeth Vintzileou, T. P. Tassios, and M Chronopoulos. Experimental validation of seismic code provisions for RC columns. *Engineering Structures*, 29(6):1153–1164, 2006.

[32] Hans I. Archundia-Aranda, Arturo Tena-Colunga, and Alejandro Grande-Vega. Behavior of reinforced concrete haunched beams subjected to cyclic shear loading. *Engineering Structures*, 49:27–42, 2013.

[33] Thomas Heitz, Cédric Giry, Benjamin Richard, and Frédéric Ragueneau. How are the equivalent damping ratios modified by nonlinear engineering demand parameters? In *6th International Conference on Computational Methods in Structural Dynamics and Earthquake Engineering*, Rhodes Island, 2017.